SAN098-1732C
SAND--98-1732C
CONF-981107--

INTEGRATED MODELING AND TESTING OF A MICRO HINGED STRUCTURE FOR SLIDING FRICTION MEASUREMENT

James M. Redmond[1], Maarten P. de Boer[2], and Terry A. Michalske[3]

Sandia National Laboratories
Albuquerque, NM 87185
[1]Structural Dynamics and Vibration Control Department MS 0439
[2]Intelligent Micromachine Department MS1080
[3]Surface and Interface Science Department MS 1413

ABSTRACT

This paper summarizes the design, modeling, and initial evaluation of a hinged structure for friction measurement in surface micromachining technology. While the area requirements are small, the present structure allows a much larger velocity and pressure range to be evaluated as compared to comb drive structures. The device consists of a cantilevered driver beam connected to a friction pad through a strategically located hinge. AC excitation of the beam flexure forces axial sliding of the friction pad due to beam foreshortening. Normal force is controlled by DC voltage on wings adjacent to the friction pad. While the achievable slip is small (10-30 nm), it is sufficient to disengage contacting asperities and engage new points of contact, and thus should be representative of frictional processes. Furthermore, the design enables the friction pad contact area to remain relatively constant over the excitation cycle. Computer simulation results are provided to mimic on-going experimental work. Increased friction forces are shown to enhance the size of hysteresis loops relating beam deflection to driver voltage.

INTRODUCTION

One of the keys to improving the reliability of MEMS devices is development of a better understanding of frictional losses and their impact on device performance. Such knowledge is critical to enhancing dynamic modeling capabilities needed to minimize the development and fabrication costs of new devices. Because they may depend on contact pressure as well as sliding velocity, however, frictional losses in the micro-domain remain difficult to quantify. While it has been shown that lightly loaded structures may exhibit very low friction in the micro-domain (Bhushan et al., 1995), significant frictional losses have been demonstrated in a moderately loaded microengine (Miller et al., 1995). Recently, two comb drive structures were built to examine the influence of lubrication on static and dynamic friction coefficients for both lateral and sidewall sliding (Srinivasan et al., 1998). Results indicate that self-assembled monolayer (SAMs) coatings greatly reduce friction for lateral sliding, and improve the life of devices featuring sidewall contacts. However, these results were derived over only a narrow range of contact pressures, and sliding velocity was not considered as a test parameter.

An alternative approach to measuring frictional losses is presented herein. The main element of the system is a cantilevered beam with a hinged friction pad. As compared to comb drive structures, this device offers greatly enhanced dynamic range in a fraction of the area. To operate, the friction pad is first brought into contact with the substrate through a DC excitation. Then, an AC excitation causes lateral deflections of the driver beam, leading to cyclic slipping of the friction pad as a consequence of beam foreshortening. This second order effect is the basic principle behind inch worm motors (Tas et al., 1997). A wide velocity range (1-1000 μm/sec) is enabled by adjusting the AC excitation frequency, while significant pressure variations (0.1 to 40 MPa) can be obtained by changing the DC friction pad voltage and altering the pad geometry. Furthermore, the apparent contact area is held relatively constant due to the action of the hinge, which minimizes rocking of the friction pad on the substrate. Hysteresis loops of beam deflection versus driver voltage contain information on frictional losses which can be deduced through dynamic modeling. All tests will be conducted in vacuum to avoid enormous losses associated with air drag and squeeze film effects (Hosaka et al., 1994)

The emphasis of this paper is on the operational principles of the hinged beam structure, in order to elucidate the model based data reduction that will be needed to infer frictional losses from test results. Toward this end, the following section describes the test apparatus. Since vibration amplitudes are limited by the well known electro-elastic instabilities (Osterberg et al, 1994), a finite element model is developed in conjunction with a distributed capacitive loading to examine tip slip amplitudes. Although electro-elastic instability becomes less predictable as the excitation frequency approaches structural resonances (Ananthasuresh et al., 1996), anticipated excitation will remain well below the structure's fundamental frequency. Depending on the driver beam length, modeling results indicate that 10-30 nm of tip slipping can

DISCLAIMER

be achieved, which is sufficient to disengage contacting asperities and engage new points of contact. Then, a double cantilevered beam model is developed that couples the longitudinally applied friction force to the electrostatically driven lateral vibration. A simulated test is described to highlight the measurable input and output quantities that will be used to extract dynamic friction coefficients. The method of extraction is a subject of on-going research that will combine experimental data with 3-d finite element modeling.

FRICTION TEST DEVICE

A schematic diagram of the MEMS friction test device (not drawn to scale) is given in Figure 1. The device consists of essentially two substructures: a flexible cantilevered beam connected to a rigid friction pad through a hinge. The basic operational principle is to engage the frictional pad with the substrate using electrostatic force resulting from DC excitation of activation pad #2. Then, AC excitation of activation pad #1 induces a bending response of the driver beam that forces slipping at the friction pad/substrate interface. The phase lag measured between the applied voltage and the beam deflection will give an indication of the frictional losses of the system.

The design of the test device represents a compromise between the requirement for substantial slip at the interface (>10nm) and the need to maintain a nearly constant contact area throughout the vibration test. The rotational stiffness of the hinge connecting the two structures is relatively high, and the relative rotation angle remains small during operation. Thus, the slope of the driver beam at the hinge is nearly zero when the friction pad is pressed against the substrate, and the driver beam behaves essentially as a double cantilevered beam with the right end clamp on rollers. Existence of the hinge, however, enables extension of the friction pad inside the span of the driver beam. This essential design element eliminates rocking of the friction pad on the substrate, thus maintaining a nearly constant apparent contact area throughout the cyclic loading phase. Only a modest pressure modulation is expected as a result of elastic deformations of the friction pad (de Boer, et al, 1998).

Gap sizes between the structure and the activation pads are kept small to produce sufficient excitation from the electrostatic forces. Once contact is made, the gap between activation pad #2 and the attractive portion of the friction pad is 1.2 micron. The nominal gap size between the driver beam and activation pad #1 ranges from 6 micron at the beam root to 4.2 micron at the hinge location, but the actual gap depends on the time varying beam deflection. During the cyclic loading phase, a maximum deflection of approximately 1.7 microns (1/3 nominal gap size) can be tolerated at the beam midpoint before electrostatic instability is encountered, and the beam snaps down to the substrate.

To demonstrate the basic operation of the device, a sample test structure with a 500 micron long driver beam is shown in Fig. 2. Both 10 and 40 volt DC excitations were used to provide differing contact pressure along the 200 micron long friction pad. Then, a 58 volt DC excitation along the driver beam was used to induce lateral deflections made evident by the fringes from a laser interferometry device. For the 10 volt friction pad excitation, a maximum lateral deflection (absolute) of 3.05 microns was measured near the driver beam mid-point. A tip slip of approximately 10 nanometers was subsequently deduced through finite element modeling coupled to an electrostatic loading function. In comparison, the 40 volt case produced only a 2.78 micron deflection of the driver beam, indicating that little slip occurred. Thus, the axial load in the beam resulting from the driver beam deformation was insufficient to overcome static friction in this case. A thorough discussion of the initial static modeling results has been previously provided (de Boer et al., 1998).

MAXIMUM SLIP ESTIMATIONS

In the absence of friction, the degree of tip sliding that can be achieved is governed solely by electrostatic instability which limits vibration amplitudes. For excitations below the driver beam's first resonant frequency, tip sliding estimates can be obtained through static instability analyses. Toward this end, structures with 500 and 250 micron driver beams with both soft (4 μm length) and stiff hinge (20 μm

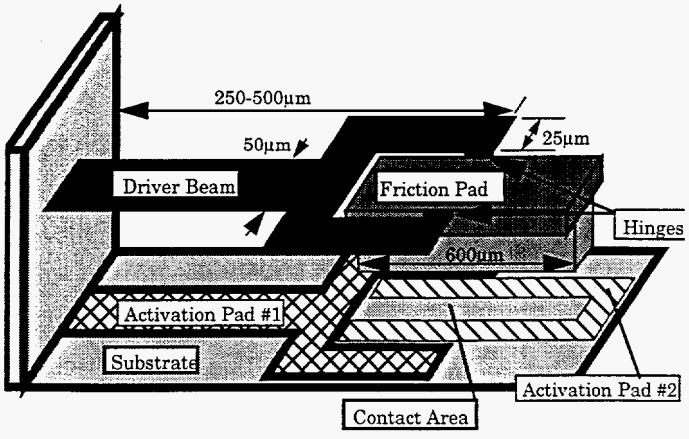

Figure 1. - Schematic diagram of MEMS frictional test device composed of cantilevered beam with hinged friction pad and dual activation pads control.

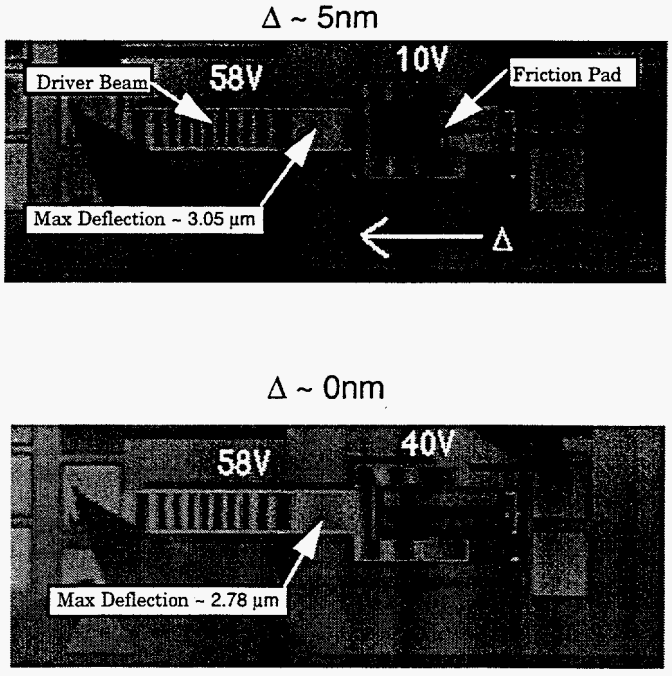

Figure 2. - Demonstration of hinged friction pad structure, illustrating the effect of friction force on beam deformations

Table 1. - Maximum Stable Static Deformations

Configuration	Voltage (V)	Deflection (μm)	Slip (nm)
500 mm, Soft Hinge	52.2	1.77	17.24
500 mm, Stiff Hinge	56.7	1.80	18.82
250 mm, Soft Hinge	170.5	1.67	23.69
250 mm, Stiff Hinge	194.5	1.77	29.57

Deformations Magnified 20x

Figure 3. - Deformed 500 μm driver beam prior to unstable snap-through.

Deformations Magnified 20x

Figure 4. - Deformed 250 μm driver beam prior to unstable snap-through.

length) connections were modeled using shell elements in Abaqus (Hibbitt, Karlsson, & Sorensen, 1996). The hinge stiffness represents a key design element. The stiffer hinge can help stave off instability, leading to greater slip distances, while the softer hinge can minimize the torque imparted to the friction pad. All degrees of freedom were fixed at the left end of the driver beams to simulate the cantilevered boundary condition. On the right end, the inside nodes of the hinges were given a prescribed lateral displacement of -1.8 microns to account for the deformation from the friction pad loading step. The associated rotational degrees of freedom were fixed while the axial and in plane displacements were left unconstrained.

A displacement dependent pressure loading routine was added to Abaqus to mimic the capacitive loading of the driver beam that results from excitation of activation pad #1. In practice, three dimensional field effects influence the capacitance of the system (Osterberg, et al., 1994), but reasonably good results were obtained for this geometry by neglecting the fringing fields

Instability calculations are summarized in Table 1. With the soft hinge, maximum attainable slip for the 500 micron beam is 17.2 nm at 52.2 V. Beyond this excitation level, the system is unstable and the driver beam snaps down to the substrate. The stiff hinge produces slightly larger slip (18.8 nm) and instability voltage limit (56.7 V). This is a consequence of the reduced rotational deformation of the driver beam in the vicinity of the hinge as shown in Fig. 3.

The effect of the stiff hinge is more dramatic for the 250 μm driver beam, with the slip increasing from 23.7 to 29.5 nanometers and the instability voltage increasing from 171 to 194 volts. These excitation levels are within the assumed operating range of 200 volts, beyond which arcing between the driver beam and the electrode can be expected. The driver beam deformations shown in Fig. 4 reveal a

marked increase in the out of plane deformations as compared to the longer driver beam. These deformations define the instability limit, but they do not contribute significantly to the axial slip. Consequently, the maximum slip of this driver beam is less than twice that of the 500 micron beam as predicted by simple beam analysis (Tas et.al., 1997).

TEST STRUCTURE MODEL

In this section, a simple dynamic model of the test structure is provided to facilitate explanation of the complex interaction of the laterally applied friction forces and the transverse vibration of the driver beam. This approach provides some fundamental insight that will aid the reduction of future test data.

Once the friction pad is brought into contact with the substrate, the overall behavior of the test device can be adequately described by the dynamics of the driver beam subject to a distributed electrostatic force and an axially applied friction load at the tip. Preliminary, finite element modeling of the entire structure indicates that the longer driver beam behaves essentially as a doubly clamped beam with slipping permitted at the right end. Thus, a uniform doubly clamped beam with rectangular cross-section shown in Fig. 5 serves as a good model for describing the qualitative behavior of the test device. The beam has length l, width b, thickness h, density ρ, and flexural rigidity EI ($I = bh^3/12$). Variable substrate height is included to mimic the differential gap size that is a consequence of the driver beam deflections from the friction pad loading step. While this step has little effect on the dynamic characteristics of the beam, it greatly influences the electrostatic force field acting on the beam, producing a distributed force per unit length $f(x,t)$. Additionally, a frictional force at the right end is included, and will be described in a later section.

Beam Dynamics

The long slender driving beam is modeled as an Euler-Bernoulli beam. Imposing the boundary conditions consistent with a doubly clamped beam yields the natural frequencies according to

$$\omega_r = (\beta_r l)^2 \sqrt{\frac{EI}{\rho b h l^4}} \tag{1}$$

in which $\beta_r l = 4.730, 7.853, 10.996....$ The mass normalized mode shapes are given by

$$\phi_r(x) = \frac{1}{\sqrt{\rho b h l}}\left[\cosh(\beta_r x) - \cos(\beta_r x) - \sigma_r(\sinh(\beta_r x) - \sin(\beta_r x))\right] \tag{2}$$

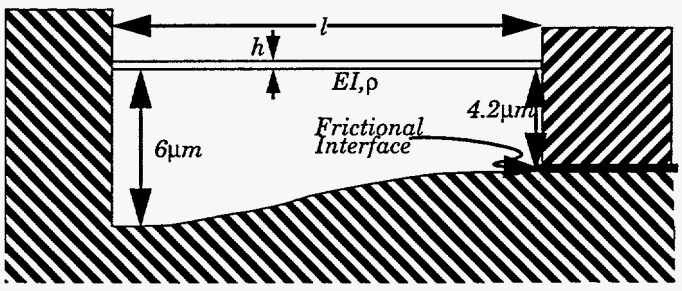

Figure 5. - Doubly clamped beam model with frictional interface and variable gap size.

with the weighting factor σ_r defined as

$$\sigma_r = \frac{\cosh(\beta_r l) - \cos(\beta_r l)}{\sinh(\beta_r l) - \sin(\beta_r l)}. \tag{3}$$

The evolution of the generalized coordinates is governed by the second order equations

$$\ddot{q}_r(t) + 2\zeta_r \omega_r \dot{q}_r(t) + \omega_r^2 q_r(t) = Q_r^{es}(t) + Q_r^{fr}(t) \tag{4}$$

in which ζ_r represents modal damping ratios that have been added to account for internal losses. Also evident in Eq. 4 are the effects of the externally applied loads $Q_r^{es}(t)$ and $Q_r^{fr}(t)$, which represent the projection of the distributed electrostatic force and the discrete frictional load onto the r^{th} mode. These two projections are now described in further detail.

Electrostatic Load

The distributed electrostatic load has a strong dependence on the gap size between activation pad #1 and the driver beam. Neglecting fringing effects, we approximate this relationship by a distributed capacitive loading as

$$f(x,t) = -\frac{1}{2}\varepsilon b \frac{V_1^2(t)}{g_1^2(x,t)} \tag{5}$$

in which ε is the permittivity of free space ($8.85\text{x}10^{-12}$ $C^2/N\text{-}m^2$), $V_1(t)$ is the time varying voltage applied to the activation pad, and $g_1(x,t)$ is the variable gap size along the beam length. The gap function is given by

$$g_1(x,t) = g_{1o}(x) + \sum_{r=1}^{\infty} \phi_r(x) q_r(t) \tag{6}$$

which exhibits dependence on both the initial gap function $g_{1o}(x)$ shown in Fig. 5 and the time varying beam deflection. This interdependence of the beam deflection and the applied load can lead to instability. For the static (or low frequency) case, maximum beam deflections are limited to 1/3 of the initial gap size, beyond which the beam will snap through and adhere to the substrate (Osterberg et al., 1994). For the test device, the initial gap size after the friction pad is loaded on the substrate can be described by the cubic deflection equation

$$g_{1o}(x) = 3.6\left(\frac{x}{l}\right)^3 - 5.4\left(\frac{x}{l}\right)^2 + 6 \qquad \mu\text{m}. \tag{7}$$

At the beam midpoint, the initial gap size is 5.1μm, giving a deflection limit at this location of 1.7 μm for low frequency excitation.

The modal excitation resulting from the applied electrostatic force is obtained by taking the inner product of the force function with the mode shapes according to

$$Q_r^{es}(t) = \int_0^l \phi_r(x) f(x,t) dx \tag{8}$$

Substituting Eqs. 5 and 6 into Eq. 8 yields the modal electrostatic forces

$$Q_r^{es}(t) = -\frac{1}{2}\varepsilon b V_1^2(t)\int_0^l \left(\frac{\phi_r(x)}{\left\{ g_{10}(x) + \sum_{r=1}^{\infty} \phi_r(x) q_r(t) \right\}^2} \right) dx \qquad (9)$$

Frictional Load

Estimating the frictional coefficient from test data requires an understanding of the mechanism through which the axially applied friction load dissipates vibrational energy in the driver beam. As stated previously, the beam model is assumed inextensible since anticipated axial deformations of the beam resulting from the friction load will be insignificant for most test configurations. Therefore, the sliding motion at the tip is attributed entirely to foreshortening resulting from the bending deformations of the beam span. This relationship is now exploited to map the frictional force to the modal dissipation.

To illustrate, we consider the classic model of sliding friction

$$F(t) = -\mu_d N sign(\dot{U}_{tip}(t)) \qquad (10)$$

in which μ_d is the coefficient of dynamic friction, N is the normal force between the friction pad and the substrate, and $\dot{U}_{tip}(t)$ is the sliding velocity of the friction pad or beam tip. While it is anticipated that the magnitude of the sliding velocity will impact the frictional force, the exact relationship is not known. Consequently, an explicit velocity dependence has been omitted in Eq. 10 for clarity. Once the exact relationship can be determined through reduction of test data, it can readily be incorporated into this model.

The size of the normal force in the test device is controlled by the voltage V_2 applied to activation pad #2. Note that some of the applied force is absorbed by the elastic deformation of the beam required to bring the friction pad into contact with the substrate. In addition, a variable reaction force will be superimposed on the normal force as the beam responds to the cyclic excitation of activation pad #1. These effects will have a negligible influence on the dissipation, and are neglected here for simplicity. The normal force is given by the electrostatic force equation

$$N = \frac{1}{2}\varepsilon A_2 \frac{V_2^2}{g_2^2} \qquad (11)$$

in which, A_2 is the area of the activation pad, and g_2 is the gap size at contact (1.2μm).

The remaining element of Eq. 10 to be examined is the axial tip velocity which assigns a direction to the friction force. Using the inextensible beam assumption, the axial tip displacements resulting from the bending deformation of the beam is given by (Segalman and Dohrmann, 1996)

$$U_{tip}(t) = -\frac{1}{2}\int_0^l \theta(x,t)^2 dx \qquad (12)$$

Here the angle θ theta is the spatial derivative of the lateral displacement

$$\theta(x,t) = \sum \phi_r'(x) q_r(t). \qquad (13)$$

Substituting Eq. 13 into Eq. 12, the tip displacement is given in terms of the modal displacements as

$$U_{tip}(t) = -\frac{1}{2}\underline{q}^T(t)\left[\int_0^l \underline{\phi}'(x)\underline{\phi}'^T(x)dx\right]\underline{q}(t). \qquad (14)$$

To simplify notation, the mode shapes and displacements in Eq. 14 have been assembled into column vectors. Note that the axial displacement of the tip is always negative, since either upward or downward deformations of the beam produce the same inward motion of the tip. Thus, the frequency of the tip motion is twice that of the lateral beam motion, provided that the beam oscillates both above and below its equilibrium. However, this complication can be eliminated by including a bias on the excitation signal, thus preventing the beam from rebounding beyond the equilibrium point. Finally, the tip velocity is obtained by taking the derivative of the displacement with respect to time, yielding

$$\dot{U}_{tip}(t) = -\dot{\underline{q}}^T(t)\left[\int_0^l \underline{\phi}'(x)\underline{\phi}'^T(x)dx\right]\underline{q}(t) \qquad (15)$$

With the normal force and directionality of the friction defined, the remaining task is to map the frictional force to the modal subspace. For this, the principle of virtual work is applied (Long, 1963)

$$\delta w = F\delta U_{tip} \qquad (16)$$

where δw represents the work done by the frictional force to move the tip through the virtual displacement δU_{tip}. The virtual work expression can be converted to an equivalent expression involving modal forces Q_r^{fr} and virtual modal displacements δq_r. From Eq. 14, the virtual tip displacement is given by

$$\delta U_{tip} = -\underline{q}^T(t)\left[\int_0^l \underline{\phi}'(x)\underline{\phi}'^T(x)dx\right]\delta\underline{q} \qquad (17)$$

Finally, substitution of Eqs. 11 and 15 into 10, and inserting the result and Eq. 17 into 16 yields the virtual work expression

$$\delta w = \underline{Q}^{frT}(t)\delta\underline{q} \qquad (18)$$

in which the vector of modal forces is given by

$$\underline{Q}^{frT}(t) = -\frac{1}{2}\mu_d \varepsilon A_2 \frac{V_2^2}{g_2^2}\left(\underline{q}^T(t)\left[\int_0^l \underline{\phi}'(x)\underline{\phi}'^T(x)dx\right]\right)X \qquad (19)$$
$$sign\left\{\dot{\underline{q}}^T(t)\left[\int_0^l \underline{\phi}'(x)\underline{\phi}'^T(x)dx\right]\underline{q}(t)\right\}$$

Examining Eq. 19., the modal forces resulting from the friction show a peculiar dependence on the modal deformations. Therefore, the

Table 2. - Sample Parameters for Example Problem.

Young's Modulus(E)	160GPa
Density (ρ)	2300 kg/m^3
Length (l)	500 μm
Width (b)	50 μm
Thickness (h)	2 μm
Natural frequency (ω_n)	69 kHz
Modal Damping Ratio (ζ)	0.02%
Activation Pad #1 Area (A_1)	25000 μm^2
Activation Pad #2 Area (A_2)	40,200 μm^2
Static Friction Coefficient (μ_s)	0.2
Dynamic Friction Coefficient (μ_d)	0.1

dissipative friction force manifests itself as a modulation of the modal stiffness. This is intuitively satisfying, since the axial applied friction load can do no work on the beam bending in the absence of deformation.

SAMPLE SIMULATIONS

For illustrative purposes, a simulation of the friction device is now presented using only the first mode of a double cantilevered beam. Beam dimensions and material parameters comparable to one of the fabricated test devices are given in Table 1. For reasons stated previously, a bias load of 22 V is added to the cyclic activation to produce only downward beam deflections.

With the friction pad voltage fixed at 50 V (N=310μN), the amplitude of the 10 KHz cyclic excitation was adjusted to maximize beam deflection amplitude without yielding a snap through instability. The steady state oscillation for the beam midpoint and the tip sliding are shown in Fig. 6. The effects of the static friction cause momentary sticking at the extreme deformation. Once the applied load decreases sufficiently, the elastic energy stored in the beam is sufficient to overcome static friction, and the beam slips free. This impulsive input gives rise to the subsequent oscillatory behavior at the natural frequency in the vicinity of the static equilibrium. Although the static friction does not influence energy dissipation per cycle, the related excitation of the beam's natural mode can complicate subsequent data reduction efforts. In practice, stiction problems can usually be overcome by increasing the frequency of excitation. The resulting increase in phase lag permits the excitation load to diminish sufficiently at max deflection to allow the elastic restoring force to immediately overcome static friction. As a consequence of the bias load, the tip slip amplitude is only about 12 nm for the 500 μm structure. Several test samples are being fabricated with a driver span of 250μm, which will permit nearly 25 nm of slipping (~1/L dependence) at increased excitation levels.

For comparison, the simulation was repeated with the friction pad voltage increased to 100 V (N=1.2mN). The cyclic excitation amplitude was increased to 38 volts to maximize beam deflection in the presence of the increased frictional losses. In comparison to the previous

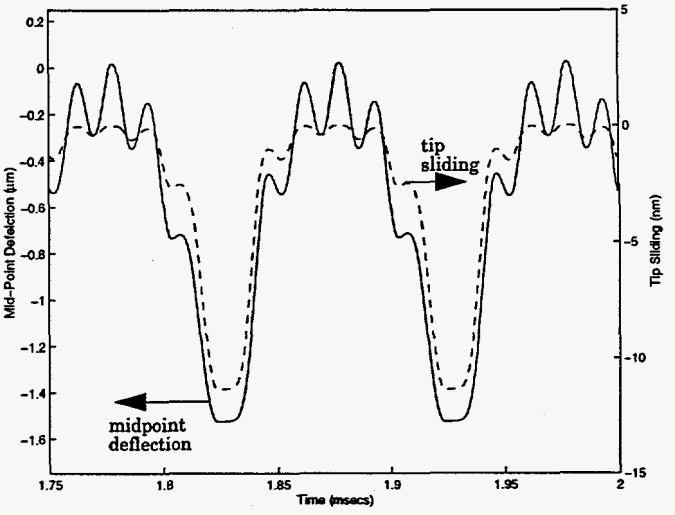

Figure 6. - Steady state vibration with V2 = 50 volts and V1 = 22+35(1+sin(ωt))/2 volts.

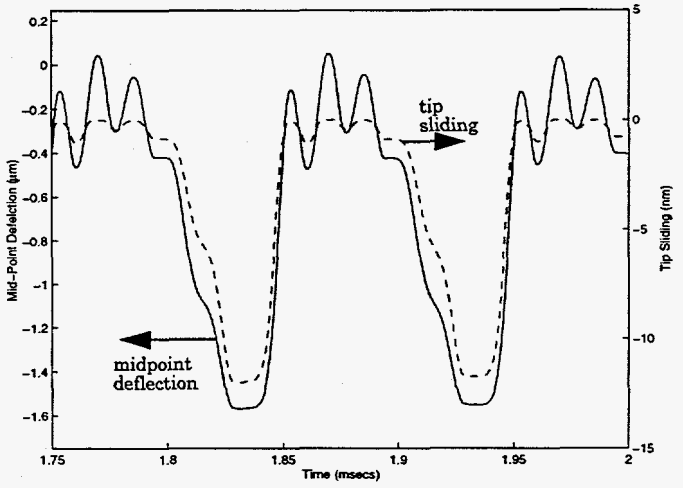

Figure 7. - Steady state vibration with V2 = 100 volts and V1 = 22+35(1+sin(ωt))/2 volts.

example, the sticking interval has increased as shown in Fig. 7, leading to increased oscillatory amplitude after slipping occurs.

A comparison of the Voltage-Displacement hysteresis loops for contact pressure excitations of 50, 100, and 200 volts are given in Fig. 8. In each case, the cyclic excitation of the driver beam was adjusted to maximize deflections without encountering instability. The hysteresis loops shown are analogous to force displacement hysteresis loops typically used to evaluate material damping (Norwick and Berry, 1972). The area contained in the loop represents the energy dissipated per cycle, and can be readily related to loss factors. Although further work is needed to determine an appropriate mapping function relating hysteresis to friction coefficient, the larger loop size resulting from increased contact pressure is direct evidence of the enhanced frictional loss.

CONCLUDING REMARKS

A summary description of the operational principle of a micro friction test device has been provided. The device, which consists of a flexible cantilevered driver beam connected to a rigid friction pad, enables examination of the influence of contact pressures and sliding velocities on frictional losses over a broad dynamic range. Maximum slip amplitude limits were estimated using a commercial finite element package coupled to a displacement dependent capacitance model to represent the electrostatic loading. Results indicated that 10-30 nm of tip slipping can be achieved depending on the configuration of the test device. A simplified beam model of a friction test device was provided in order to elucidate the complex coupling mechanism between the dissipative frictional forces and the structural response. Foreshortening resulting from bending vibrations of the driver beam gives rise to slipping at the beam tip, introducing frictional losses into the system. While further work is needed to determine an appropriate relationship between measurable test parameters and friction coefficients, the single degree of freedom examples presented reveal a correlation between contact pressure and hysteresis. Additional testing techniques for determining friction coefficients will also be considered, including resonance testing and free decay. Experimental verification and evaluation of this device is currently underway and will be reported in future symposia.

ACKNOWLEDGMENTS

The authors appreciate the assistance of Clark Dohrmann of Sandia for his help in modeling the influence of the tip sliding friction on the bending vibration.

REFERENCE

"Abaqus/Standard User's Manual," 1996, Version 5.6, Hibbitt, Karlsson,& Sorensen, Inc, Pawtuckett, Rhode Island.

Ananthasuresh, G.K., Gupta, R.K., and Senturia, S.D., 1996, "An Approach to Macromodeling of MEMs for Nonlinear Dynamic Simulation," ASME DSC-Vol.59, pp. 401-407.

Bhushan, B., Israelachvili, J.N., and Landman, U, 1995, "Nanotribology: Friction Wear and Lubrication on the Atomic Scale," Nature, Vol. 374, No. 13, pp. 607-616.

de Boer, M.P., Redmond, J.M., Michalske, T.A., 1998, "A Hinged Pad Test Structure for Sliding Friction Measurement in Micromachining," Proceedings of the SPIE 1998 Symposium on Micromachining and Microfabrication, Santa Clara, CA.

Hosaka, H., Itao, K., and Kuroda, S, 1994, "Evaluation of Energy Dissipation Mechanisms in Vibrational Microactuators," Transactions of IEEE, 0-7803-1833-1, pp. 193-198.

Long, R.R., 1963, Engineering Sciences Mechanics, Prentice Hall, Englewood Cliffs, New Jersey, 1963.

Miller, S.L., Sniegowski, J.J., LaVigne, G., and McWhorter, P.J., "Friction in Surface Micromachined Microengines,"

Nowick, A.S. and Berry, B.S., *Anelastic Relaxation in Crystalline Solids*, Academic Press, New York, New York, 1972.

Osterberg, P.M., Gupta, R.K., Gilbert, J.R., and Senturia, S.D., 1994, "Quantitative Models for the Measurement of Residual Stress, Poisson Ratio, and Young's Modulus Using Electrostatic Pull-in of Beams and Diaphragms," Solid State Sensor and Actuator Workshop, Hilton Head South Carolina, pp. 184-188.

Segalman, D.J., Dohrmann, C.R., 1996, "A Method for Calculating the Dynamics of Rotating Flexible Structures, Part:1: Derivation," Journal of Vibration and Acoustics, Vol. 118, pp. 313-317.

Srinivasan, U., Foster, J.D., Habib, U., Howe, R.T., Maboudian, R., Senft, D.C., and Dugger, M.T., 1998, "Lubrication of Polysilicon Micromechanisms With Self-Assembled Monolayers," Proceedings of Hilton Head.

Tas, N. Wissink, J. Sander, L.,Lammerink, T., and Elwenspoek, M., 1997, "The Shuffle Motor: A High Force, High Precision Linear Elastic Stepper Motor," Transducers '97, International Conference on Solid State Sensors and Actuators, Chicago, IL, pp. 777-780.

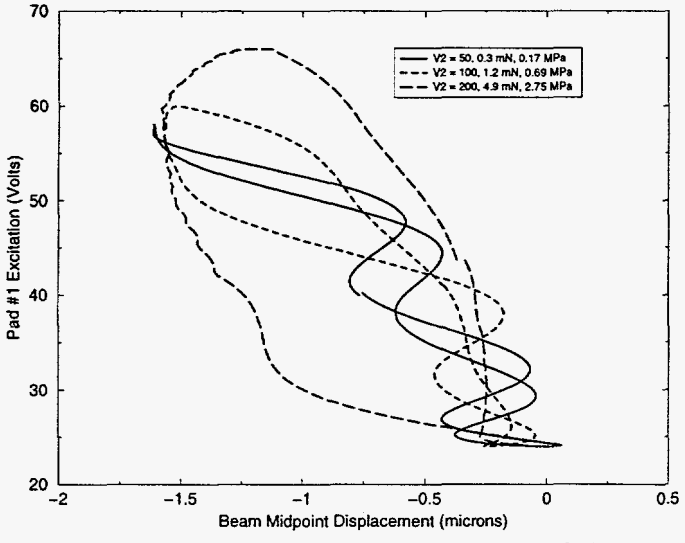

Figure 8. - Displacement versus voltage hysteresis loops for various contact pressures.

Sandia is a multiprogram laboratory operated by Sandia Corporation, a Lockheed Martin Company, for the United States Department of Energy under contract DE-AC04-94AL85000.